Petroleum Science 23 (2026) 1469–1486

Contents lists available at ScienceDirect

Petroleum Science

journal homepage: www.keaipublishing.com/en/journals/petroleum-science

Original Paper

A numerical study on blending hydrogen into natural gas pipeline by the SMV static mixer: Mixing performance and mass transfer mechanism

Tao Di [a], Xu Sun [a,*], Peng-Chao Chen [b,**], Hong-Yu Zhou [a], Qi-Yu Huang [a], Xiao-Ben Liu [a]

[a] National Engineering Research Center for Pipeline Safety, MOE Key Laboratory of Petroleum Engineering, Beijing Key Laboratory of Urban Oil and Gas Distribution Technology, China University of Petroleum (Beijing), Beijing, 102249, China
[b] PipeChina Institute of Science and Technology, Tianjin, 300450, China

ARTICLE INFO

Article history:
Received 12 May 2025
Received in revised form
7 August 2025
Accepted 18 November 2025
Available online 22 November 2025

Edited by Teng Zhu

Keywords:
Natural gas pipeline
Static mixer
Large eddy simulation
Hydrogen blending transportation
Mixing homogeneity

ABSTRACT

Hydrogen is an important clean energy carrier that contributes to the carbon neutrality by reducing the dependence on fossil fuels. As its role in the global energy system continues to expand, the demand for the hydrogen blended natural gas transportation is steadily rising, which brings a new challenge of the uniform mixing for the safe and efficient long-distance transmission. In this study, the mixing performance of the Sulzer SMV static mixer for hydrogen blending in natural gas pipelines is investigated numerically. Using the large eddy simulation method, and a detailed parametric analysis of geometric factors including element orientation, aspect ratio, twist angle, and spacing are conducted. The results indicate that the SMV mixer markedly enhances the mixing of hydrogen and methane. Increasing the number of mixing elements from one to six improves the mixing homogeneity but causes a 4.5 times increase in the pressure drop. The flow field visualization and vortex evolution analyses demonstrate that vortex generation plays a dominant role in fluid disturbance and mixing enhancement, with Dean vortices being particularly effective in promoting hydrogen and methane blending. This study provides valuable guidance for the design and optimization of static mixing devices, thereby advancing the hydrogen utilization and improving energy efficiency in sustainable energy systems.

* Corresponding author.
** Corresponding author.
E-mail addresses: xsun@cup.edu.cn (X. Sun), chenpc@pipechina.com.cn (P.-C. Chen).
Peer review under the responsibility of China University of Petroleum (Beijing)

https://doi.org/10.1016/j.petsci.2025.11.036

Nomenclature

$L_{(in)}$	Length of natural gas pipeline upstream of blending point
$L_{(H2)}$	Length of the hydrogen pipeline
L_e	Length of the static mixer
d	Diameter of the hydrogen pipeline
α	Twist angle of corrugated plate
h	Height of the corrugated plate
x^*	Downstream distance from the static mixer outlet
COV	Coefficient of variation
i	Number of mesh nodes at the section
c	Average mole fraction of hydrogen in the entire section
V	Vertical
$L_{(out)}$	Length of gas pipeline downstream of blending point
L_a	Length from the blending point to the static mixer inlet
D	Diameter of the natural gas pipeline
D_e	Diameter of the SMV static mixer
s	Height of the corrugated plate spacing
x	Length along the flow direction of the natural gas pipeline
L^*	Distance from the static mixer inlet to the mixer interior
P	Pressure drop
c_i	Hydrogen mole fraction of the i-nodes at the section
Ar	Aspect ratio
H	Horizontal

1. Introduction

With the advancement of modern technologies and the growing demand for high-quality products (Liu et al., 2025), the efficient mixing has become increasingly important in a wide range of industries (Kouadri et al., 2021; Chen et al., 2023). In processes such as the petroleum production, chemical processing, and biological industry, the need for effective mixing solutions is constantly growing to meet goals of both quality standards and environmental sustainability (Guo et al., 2023; Ruan et al., 2024). As industries evolve, optimizing mixing processes not only enhances production efficiency but also helps to reduce energy consumption and minimize waste, contributing to global efforts toward sustainability and carbon reduction (Yang et al., 2024b). Due to the complexity of mixing processes, selecting an appropriate mixing device is essential to prevent inefficiencies that may compromise both process performance and safety (Vashisth et al., 2021; Delaplace et al., 2023).

The main types of mixing equipment are dynamic mixers and static mixers. Dynamic mixers employ mechanical agitation to blend materials, achieving rapid mixing and efficient mass transfer (Horie et al., 2011; Casugbo and Baker, 2018; Shi et al., 2020). They are particularly advantageous for processes that require high shear rates; however, their reliance on moving parts often leads to higher energy consumption and greater maintenance requirements (Bennour et al., 2023). In contrast, static mixers employ fixed mixing elements positioned within a tubular structure to promote efficient mixing (Zidouni et al., 2015). Instead of relying on mechanical agitation, they enhance mixing by disrupting the flow as it passes through the elements, generating turbulence that strengthens interfacial interactions (Rabha et al., 2015). This mechanism induces chaotic convection, substantially enlarging the effective mixing area and enabling improved blending even under low-flow conditions (Zhang et al., 2019; Gao et al., 2024). The absence of moving parts in static mixers minimizes maintenance requirements and reduces energy consumption (Albertazzi et al., 2024). These advantages make static mixers highly applicable across a wide range of industrial mixing processes (Zhuang et al., 2020).

In response to the global pursuit for green and low-carbon energy solutions, blending hydrogen into existing natural gas pipelines has emerged as an effective approach to decarbonize current energy infrastructure while minimizing retrofitting costs (Chen et al., 2025; Lu et al., 2025). This approach enables the gradual integration of hydrogen into energy systems by utilizing the existing natural gas infrastructures (Shi et al., 2023; Ichikawa, 2024; Wu et al., 2024a). However, achieving effective mixing of hydrogen and natural gas remains a challenge because of their pronounced differences in physical properties (An et al., 2023; Yan et al., 2023; Zhao and Cheng, 2024). Notably, the much lower density of hydrogen compared to natural gas may cause gas stratification when blended through conventional T-junctions (Eames et al., 2022; Liu et al., 2023a; Khabbazi et al., 2024; Ouyang et al., 2024), resulting in localized hydrogen-rich zones. This non-homogeneity not only increases the risk of hydrogen-induced embrittlement in pipelines (Jia et al., 2023), but also reduces metering accuracy and complicates leak detection (Zheng et al., 2025). Natural convection and molecular diffusion are generally insufficient to overcome this stratification. Moreover, the high molecular diffusivity of hydrogen results in steep concentration gradients near the injection point, further impeding rapid and homogeneous mixing. Compared with other gas mixtures of similar properties, the hydrogen–methane system exhibits considerably greater complexity. Although adjusting the injection orientation can mitigate stratification to some extent, achieving homogeneous mixing under practical engineering conditions remains a great challenge (Wu et al., 2024b; Ali and Tormene, 2025; Rosa et al., 2025). Therefore, dedicated design and optimization of mixing devices are essential to achieve homogeneous blending and to ensure the safe and stable operation of hydrogen-blended natural gas systems.

Advances in static mixer technology provide a promising pathway for the safe and efficient integration of hydrogen into natural gas pipelines. The performance of a static mixer is closely related to the physical properties of the blended gases and the corresponding operational requirements. Therefore, the selection of an appropriate mixer should be guided by the specific application scenario, as different mixer types offer distinct advantages in terms of mixing efficiency, pressure drop, and structural adaptability (Valdés et al., 2022). To date, numerous static mixer configurations have been developed and investigated for blending hydrogen into natural gas networks, each exhibiting unique design features and performance characteristics. As summarized in Table 1, Liu et al. (2023b) investigated the mixing performance of the SMX static mixer, with numerical simulations validated by experimental results, and recommended using four mixing elements for optimal performance. Subsequently, Zheng et al. (2024) proposed a coaxial shear static mixer featuring ring-shaped structures, whose mixing homogeneity and pressure drop performance were found to surpass those of the SMX mixer (Liu et al., 2023b). Liu et al. (2022) examined the blending behavior of different natural gas sources using four types of static mixers

Table 1
Overview of previous studies on static mixers for hydrogen blending.

Scholar	Static mixer	Method	Hydrogen blending ratio	Key results
Fernandes et al. (2024)	KMS and KVM	CFD	5%–20%	Compared to the KMS static mixer, the KVM demonstrates superior performance in terms of both mixing efficiency and pressure drop.
Zheng et al. (2024)	Coaxial shear	CFD	5%–25%	When the number of cavities increases to 48, the mixing homogeneity reaches 95.43%, and the pressure drop is 67.02 Pa.
Kong et al. (2021)	Helical	CFD/Experimental	20%	Three mixing elements offers an optimal trade-off between mixing performance and pressure drop. The 120° angle yields the best mixing performance.
Wang et al. (2025)	Self-designed	CFD/Experimental	5%–25%	Mixing homogeneity can be improved by using this static mixer. While pressure has little effect on mixing performance, increasing the hydrogen ratio or flow rate initially enhances homogeneity, peaking at 10% hydrogen and 10 m^3/h, before declining.
Liu et al. (2023b)	SMX	CFD/Experimental	0%–30%	An increase in the hydrogen volume fraction enhances mixing homogeneity but also results in a slight rise in pressure drop. Hydrogen blending experiments can be performed using nitrogen as a surrogate for natural gas.
Di et al. (2024)	Self-designed	CFD	5%–20%	Optimal mixing was achieved when the static mixer with 4 mixing elements was installed 3 diameters downstream of the blending point, with a spacing of 1 diameter between the mixing elements.
Yang et al. (2024a)	LPD, Y-type and double-jet vortex	CFD	5%–20%	Mixing homogeneity improves with increasing flow velocity, hydrogen blending ratio, twist angle, and number of mixing elements, as well as with a decreasing aspect ratio.
Ali and Tormene (2025)	Modular	CFD	1%–20%	The mixer consistently achieved high mixing homogeneity with low pressure drop (<2.2 bar).
Zheng et al. (2025)	Kenics static mixer	CFD/Experimental	5%–25%	Pipeline pressure and temperature changes have a minimal impact on the mixing characteristics.

through numerical simulations, and reported that the spiral vane mixer achieved the best mixing performance among the tested configurations. Building on helical and LPD static mixer concepts, Yang et al. (2024a) designed five different static mixers for the hydrogen-methane blending. The results indicated that the new LPD static mixer achieved the best mixing performance, which is consistent with the findings of Su et al. (2023). In a related study, Fernandes et al. (2024) employed a helicoidal mixer (KMS), a KVM mixer and a standard T-junction to blend hydrogen into natural gas pipelines. Their results showed that the KVM mixer achieved the required mixing homogeneity within 7 pipe diameters, whereas the KMS required 13. Wang et al. (2025) combined numerical simulation and experimental approaches to design and optimize a static mixer structure for hydrogen blending, with the sampling point arrangement refined based on the work of Liu et al. (2023b). Zheng et al. (2025) conducted Computational fluid dynamics (CFD) simulations and experimental validation to evaluate the mixing performance of hydrogen and natural gas in a Kenics static mixer. They identified an optimal configuration consisting of two helical elements with a 135° twist angle and a length-to-diameter ratio of 2, which provided the best balance between the mixing efficiency and pressure drop. These studies collectively underscore the critical influence of geometric parameters on the static mixer performance. Furthermore, Ali and Tormene (2025) developed and tested a modular static mixing system suitable for various hydrogen blending concentrations. Their system maintained a consistently low pressure drop across the 1%–20% hydrogen blending range. Notably, its successful implementation in the Green Hysland project in Palma de Mallorca demonstrated the reliable real-world performance and confirmed the practicality of the design under actual operating conditions.

As reviewed above, previous studies have examined a large number of static mixers, including SMX, LPD, and Kenics types, for hydrogen blending in natural gas pipelines. These mixers exhibit distinct advantages and limitations depending on specific mixing objectives such as the homogeneity, pressure drop, and structural integration. Some configurations have demonstrated favorable performance in enhancing gas-phase mixing and have been gradually incorporated into hydrogen blending applications, while the SMV static mixer has received comparatively little attention. Originally developed by Sulzer in the 1970s, the SMV mixer consists of a series of stacked corrugated plates that form open and intersecting channels, which divides the main flow into multiple substreams and generates a turbulent flow field with high levels of homogeneity and isotropy (Schrimpf et al., 2019). The SMV mixer is particularly attractive for gas-phase applications due to its simple geometry and low manufacturing cost (Etchells III and Meyer, 2003; Paglianti and Montante, 2013). To the best of our knowledge, however, the effects of its geometric parameters on flow dynamics, mixing efficiency, and pressure drop have not yet

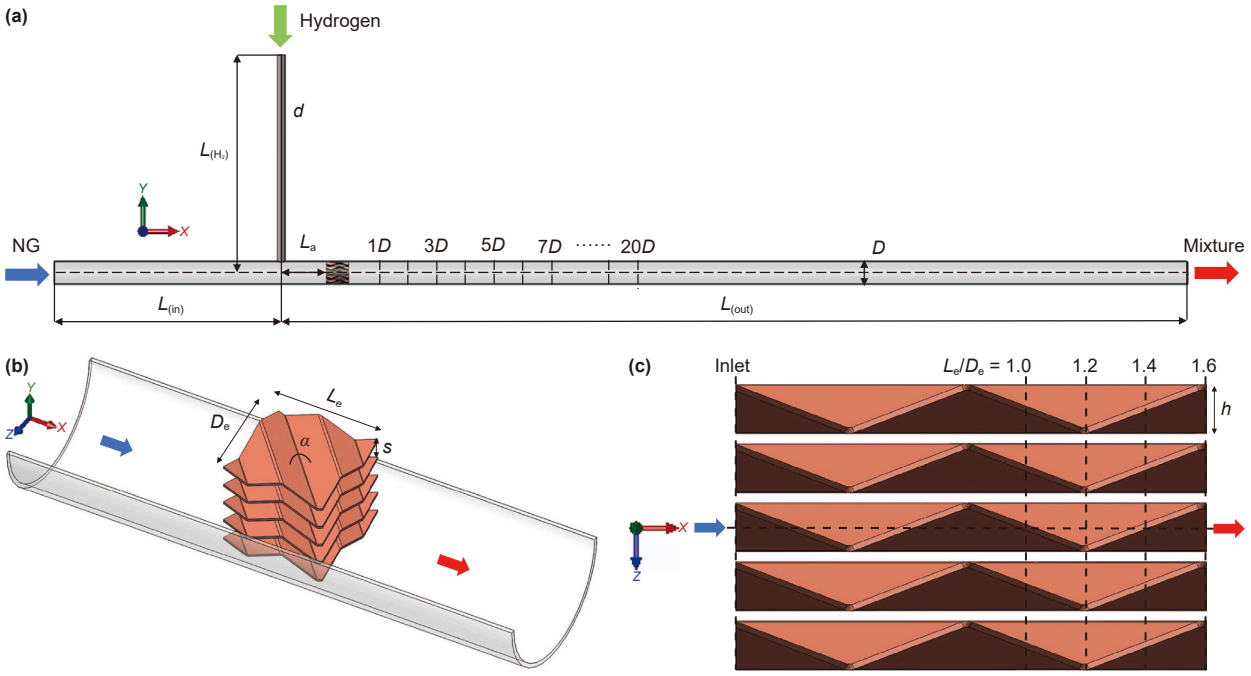

Fig. 1. Geometry of natural gas pipeline with the SMV static mixer.

been thoroughly investigated. This lack of fundamental understanding presents a significant obstacle to evaluating its feasibility for engineering implementation in hydrogen blending systems.

This study aims to address the existing research gap concerning the application of SMV static mixers for hydrogen blending in natural gas pipelines. A series of numerical simulations were conducted to systematically investigate the effects of key geometric parameters on the mixing performance and associated pressure drop of SMV static mixers. The evaluation indices included the coefficient of variation of gas concentration and the pressure drop across the mixer. Furthermore, the influence of the number of mixing elements on the mixing efficiency was explored. Finally, a detailed flow field analysis was conducted to elucidate the fundamental mixing mechanisms, providing a deeper insight into the vortex structures and flow patterns involved in the process. The findings provide theoretical guidance for the rational design and optimization of SMV static mixers, thereby supporting the safe, efficient, and standardized deployment of hydrogen blending within existing natural gas infrastructure.

2. Mechanics model and mathematical formulation

2.1. Mechanics model

Fig. 1 illustrates the geometry of the natural gas pipeline equipped with the SMV static mixer. As seen in Fig. 1(a), the model consists of three main components: a natural gas pipeline with a total length of $L_{(in)} + L_{(out)}$ and a diameter D; a hydrogen injection pipeline with a length $L_{(H2)} = L_{(in)}$ and a diameter d; and the SMV static mixer. An axial distance of $L_a = 2D$ is defined between the hydrogen blending point and the entrance of the static mixer. This spacing enables the hydrogen jet to preliminarily mix with the natural gas before entering the mixer, promoting a more uniform velocity and concentration profile at the inlet. It also provides sufficient space for the installation, inspection, and maintenance of the device in practical pipeline applications. The blue, green, and red arrows indicate the flow directions of the natural gas, hydrogen, and the resulting mixture, respectively. To assess the mixing effectiveness, twenty cross-sections are extracted downstream of the mixer, each separated by one diameter ($1D$).

As shown in Fig. 1(b), the SMV static mixer comprises five stacked corrugated plates. Each plate is defined by its length L_e, width D_e, height h, twist angle α, and inter-plate spacing s. Fig. 1(c) illustrates the configuration of the mixing elements at different aspect ratios. The detailed geometric parameters of the model and the simulation conditions are listed in Tables 2 and 3, respectively.

2.2. Mathematical formulation

The Large Eddy Simulation (LES) method was employed in this study to solve the continuity, momentum, energy and species transport equations. The fundamental approach of LES involves spatially filtering turbulent motion and separating it into large scales (resolved scales) and small scales (sub-grid-scales, SGS). The large-scale structures are resolved directly, while the influence of the unresolved SGS motions on the resolved scales is modeled using appropriate SGS models (Gao et al., 2022). Based on the fundamental principles of LES, the filtered governing equations for

Table 2
Specific parameter of SMV static mixer.

Parameter	Symbol	Unit	Value
Length of NG pipeline	$L_{(in)} + L_{(out)}$	mm	5000
Length of H_2 pipeline	$L_{(H2)}$	mm	1000
Length of location of SMV static mixer	L_a	mm	200
Length of static mixer	L_e	mm	Varied
Diameter of NG pipeline	D	mm	100
Diameter of H_2 pipeline	d	mm	30
Width of static mixer	D_e	mm	98
Twist angle	α	°	Varied
Spacing between corrugated plates	s	mm	Varied
Height of each corrugated plate	h	mm	16.4

Table 3
Working conditions.

Case	Orientation	Aspect ratio L_e/D_e	Height ratio s/h	Angle, °	Number of elements	Velocity of methane, m/s	Pressure, MPa
1	Horizontal (H)	1.0	1.2	120	1	5	4
2	Vertical (V)	1.0	1.2	120	1	5	4
3	V	1.2	1.2	120	1	5	4
4	V	1.4	1.2	120	1	5	4
5	V	1.6	1.2	120	1	5	4
6	V	1.0	1.2	90	1	5	4
7	V	1.0	1.2	60	1	5	4
8	V	1.0	1.2	45	1	5	4
9	V	1.0	0.8	90	1	5	4
10	V	1.0	0.6	90	1	5	4
11	HV	1.0	1.2	120	2	5	4
12	HVHV	1.0	1.2	120	4	5	4
13	HVHVHV	1.0	1.2	120	6	5	4

compressible gas flow can be expressed as follows (Liu and Liu, 2024):

$$\begin{cases} \dfrac{\partial\overline{\rho}}{\partial t}+\dfrac{\partial\left(\overline{\rho}\tilde{u}_i\right)}{\partial x_i}=0 \\ \dfrac{\partial\left(\overline{\rho}\tilde{u}_i\right)}{\partial t}+\dfrac{\partial\left(\overline{\rho}\tilde{u}_i\tilde{u}_j\right)}{\partial x_j}+\dfrac{\partial\overline{p}}{\partial x_i}=\dfrac{\partial}{\partial x_j}\left[\tilde{\tau}_{ij}-\overline{\rho}\left(\widetilde{u_iu_j}-\tilde{u}_i\tilde{u}_j\right)\right] \\ \dfrac{\partial\left(\overline{\rho}\tilde{h}_s\right)}{\partial t}+\dfrac{\partial}{\partial x_i}\left(\overline{\rho}\tilde{u}_i\tilde{h}_s\right)=\dfrac{\partial\overline{p}}{\partial t}+\tilde{u}_i\dfrac{\partial\overline{p}}{\partial x_i}+\dfrac{\partial}{\partial x_i}\left[\lambda\dfrac{\partial\tilde{T}}{\partial x_i}-\overline{\rho}\left(\widetilde{u_ih_s}-\tilde{u}_i\tilde{h}_s\right)\right] \\ \qquad +\overline{\tau}_{ij}\dfrac{\partial\tilde{u}_i}{\partial x_j}-\dfrac{\partial}{\partial x_i}\left(\overline{\rho}\sum_{k=1}^{N}V_{k,i}Y_kh_{s,k}\right) \end{cases} \tag{1}$$

where the over-bar "–" denotes physical spatial filtered variable, $\overline{f}(x)=\int G(x,x')f(x')\mathrm{d}x'$, and tilde "~" denotes a Favre-averaged filtered variable, $\tilde{f}=\overline{\rho f}/\overline{\rho}$. ρ is the fluid density, u_i is the i-th component of the velocity vector, P is the fluid pressure, h_s is the sensible enthalpy, $V_{k,i}$ is the diffusion velocity of the k-th species, $q_i=\lambda\frac{\partial T}{\partial x_i}$ is the heat flux vector, T is the fluid temperature, and λ is the thermal conductivity.

The total stress tensor τ_{ij} can be given by:

$$\tau_{ij}=\mu\left[\frac{\partial\tilde{u}_i}{\partial x_j}+\frac{\partial\tilde{u}_j}{\partial x_i}\right]-\left(\frac{2}{3}\mu\frac{\partial\tilde{u}_k}{\partial x_k}\right)\delta_{ij} \tag{2}$$

The Dynamic Smagorinsky Model (DSM) has been demonstrated to be more suitable for computing gas mixing processes in pipelines than other models, as reported in our previous studies (Di et al., 2024). Therefore, the DSM was adopted in this study to accurately capture the small-scale vortex structures (Hoque et al., 2024).

$$\tau_{ij}^{\mathrm{SGS}}-\frac{1}{3}\delta_{ij}\tau_{kk}^{\mathrm{SGS}}=-2\nu_{\mathrm{SGS}}\tilde{S}_{ij} \tag{3}$$

In Eq. (3), S_{ij} is the strain rate tensor in resolved scales and ν_{SGS} is SGS eddy viscosity coefficient (Mirfasihi et al., 2025), which can be computed by:

$$\nu_{\mathrm{SGS}}=(C_s\Delta)^2\left|\tilde{S}\right| \tag{4}$$

$$\tilde{S}_{ij}=\frac{1}{2}\left(\frac{\partial\tilde{u}_i}{\partial x_j}+\frac{\partial\tilde{u}_j}{\partial x_i}\right) \tag{5}$$

$$C_s{}^2=\frac{\langle L_{ij}M_{ij}\rangle}{\langle M_{ij}M_{ij}\rangle} \tag{6}$$

$$M_{ij}=2\Delta^2\left(\left|\tilde{S}\right|\tilde{S}_{ij}-\widetilde{\left|\tilde{S}\right|\tilde{S}_{ij}}\right) \tag{7}$$

$$L_{ij}=\widetilde{\tilde{u}_i\tilde{u}_j}-\tilde{\tilde{u}}_i\tilde{\tilde{u}}_j \tag{8}$$

where, C_s is dynamic Smagorinsky constant, $\Delta=\sqrt[3]{\Delta_x\Delta_y\Delta_z}$ is the grid filter width, L_{ij} is the resolved Leonard stress tensor, Δ_x, Δ_y, Δ_z represent the cell size in the respective coordinate direction, "⟨⟩" stands for averaging operation, and $\left|\tilde{S}\right|=\sqrt{2\tilde{S}_{ij}\tilde{S}_{ij}}$ is the filter size.

The filtered transport equation for the mass fraction of the k-th species is expressed as follows

$$\frac{\partial\left(\overline{\rho}\tilde{Y}_k\right)}{\partial t}+\frac{\partial}{\partial x_i}\left(\overline{\rho}\tilde{u}_i\tilde{Y}_k\right)=\frac{\partial}{\partial x_i}\left[\overline{V_{k,i}Y_k}-\overline{\rho}\left(\widetilde{u_iY_k}-\tilde{u}_i\tilde{Y}_k\right)\right] \tag{9}$$

The right-hand side term in the species transport equation needs to be closed:

$$\widetilde{u_iY_k}-\tilde{u}_i\tilde{Y}_k=-\frac{\mu_t}{\mathrm{Sc}_t}\frac{\partial\tilde{Y}_k}{\partial x_i} \tag{10}$$

$$\overline{V_{k,i}Y_k}=-\overline{\rho}\overline{D}_k\frac{\partial\tilde{Y}_k}{\partial x_i} \tag{11}$$

where Y_k is the mass fraction of species $k=1,\ldots,N$, D_k is the molecular diffusion coefficient, and Sc_t is the SGS Schmidt number for species k.

2.3. Evaluation indices

Mixing homogeneity and pressure drop are commonly used to evaluate the performance of static mixers. Mixing homogeneity is

quantified by the coefficient of variation (*COV*), which represents the uniformity of component distribution within the fluid. A lower *COV* value indicates a higher degree of mixing homogeneity. According to Bie et al. (2025), the *COV* can be calculated by:

$$COV = \frac{1}{\overline{c}}\sqrt{\sum_{i=1}^{n}\frac{(c_i-\overline{c})^2}{n-1}} \times 100\% \tag{12}$$

where c_i is the hydrogen mole fraction at node i, $\overline{c}$ is the mean mole fraction, and n is the number of sampling points on the cross-section.

In conventional mixing applications, a *COV* less than 5% is generally considered indicative of homogeneous mixing. However, because hydrogen possesses an exceptionally high diffusion coefficient and a much lower molecular weight than methane, its mixing behavior differs markedly from that of typical chemical fluids. Consequently, a more stringent criterion is often applied for hydrogen-natural gas systems, where a *COV* threshold below 2% is regarded as necessary to ensure the adequate mixing homogeneity (Kong et al., 2021).

The pressure drop is defined as the difference between the area-averaged pressures at the inlet and outlet cross-sections, which can be expressed as

$$\Delta P = P_{\text{inlet}} - P_{\text{outlet}} \tag{13}$$

where P_{inlet} and P_{outlet} denote the area-averaged pressure. In this study, the area-averaged pressure over a surface A is calculated as

$$P = \frac{\int_A P\mathrm{d}A}{\int_A \mathrm{d}A} \tag{14}$$

This approach ensures that local pressure variations across the surface are accounted for, providing a reliable estimate of the overall flow resistance.

3. Numerical methods

3.1. Simulation methods

A three-dimensional, double-precision, and segregated solver was employed to conduct the simulations in this study. To accurately resolve the pressure and velocity fields under compressible and transient conditions, the Pressure-Implicit with Splitting of Operators (PISO) algorithm was applied. This approach ensured the numerical stability and accuracy in simulating complex fluid dynamics. Gravitational acceleration was set to 9.81 m/s^2 along the negative y-axis. A time step of 10^{-4} was adopted to maintain the Courant–Friedrichs–Lewy (CFL) number below 1, thereby ensuring temporal accuracy and stability. Convergence was monitored using the residuals of the velocity components and continuity equation, with convergence criteria set to 10^{-6} for continuity and 10^{-5} for all other variables.

Both the methane and hydrogen inlets were defined as the velocity inlets. The primary flow consisted of pure methane entering at a velocity of 5 m/s and a temperature of 300 K, while the secondary flow introduced pure hydrogen at 6.173 m/s and 300 K, corresponding to a hydrogen blending ratio of 10%. The pipeline outlet was set as the pressure outlet (4 MPa). A no-slip boundary condition was applied to all walls. Furthermore, time-averaged flow statistics were recorded after the flow field reached a statistically steady state.

3.2. Model validation

To validate the accuracy of the mathematical model and numerical approach described above, a T-junction model was employed, as shown in Fig. 2(a). The model geometry and operating conditions were consistent with those in the experiment (Fernandes et al., 2024), with diameters of 0.08 m for the natural gas pipeline and 0.032 m for the hydrogen pipeline. The flow velocity, hydrogen blending ratio and operating pressure were set to 20 m/s, 20%, and 1.8 MPa, respectively. LES results were compared with the experimental data at $x/D = 10$ and $x/D = 30$. As illustrated in Fig. 2(b) and (c), the simulation exhibited good agreement with the experimental measurements, with average relative deviations of 3.4% for the pressure drop and 5.8% for the *COV* of hydrogen concentration. These results confirm the reliability of the proposed numerical method for simulating hydrogen–natural gas mixing in pipelines.

3.3. Mesh generation and independence analysis

The accuracy of numerical simulations is highly sensitive to the mesh resolution. To balance computational cost and accuracy, four mesh configurations were generated, containing 920,269, 1,285,042, 1,969,124, and 2,400,248 cells, respectively. The computational mesh is shown in Fig. 3(a). The boundary layer inflation was applied near walls with a growth rate of 1.1 to resolve near-wall gradients, and the dimensionless wall distance ($y+$) was maintained below 1.0 to meet LES requirements. The mesh quality was evaluated using two widely accepted metrics: maximum skewness and orthogonal quality, the skewness reflects how much a cell deviates from an ideal shape, and values above 0.85 may lead to numerical instability. In this study, the maximum skewness was kept below 0.6, indicating well-shaped elements. The orthogonal quality measures the alignment between cell faces and the line connecting adjacent cell centers; values closer to 1 are ideal, whereas values below 0.2 are typically unacceptable. The minimum orthogonal quality in the present mesh exceeded 0.4, confirming satisfactory mesh quality. Additionally, the mesh refinement was applied around the internal structures of the static mixer to enhance local resolution in regions with steep velocity and concentration gradients, which ensured adequate resolution of vortex dynamics and scalar transport phenomena that are critical to accurately capturing the hydrogen–methane mixing process.

The geometry and boundary conditions correspond to Case 1 in Table 3. The simulations were conducted using a high-performance Dell R750XS workstation with dual Intel Xeon Gold 6338 CPUs (2.0 GHz, 32 cores) and 256 GB RAM. For the finest mesh (2,400,248 cells), the transient simulation with a time step of 0.1 ms and a total simulated time of 12 s required approximately 180 h. In contrast, the coarsest mesh (920,269 cells) required 100 h under the same conditions. Simulation results for different meshes are shown in Fig. 3(b) and (c), where the horizontal axis denotes the ratio of the distance from the mixing element exit (x^*) to the pipeline diameter (D), and the vertical axis represents pressure drop and hydrogen mass fraction, respectively. When the number of cells exceeded 1,969,124, the pressure drop remained virtually unchanged, and the average deviation in mass fraction was only

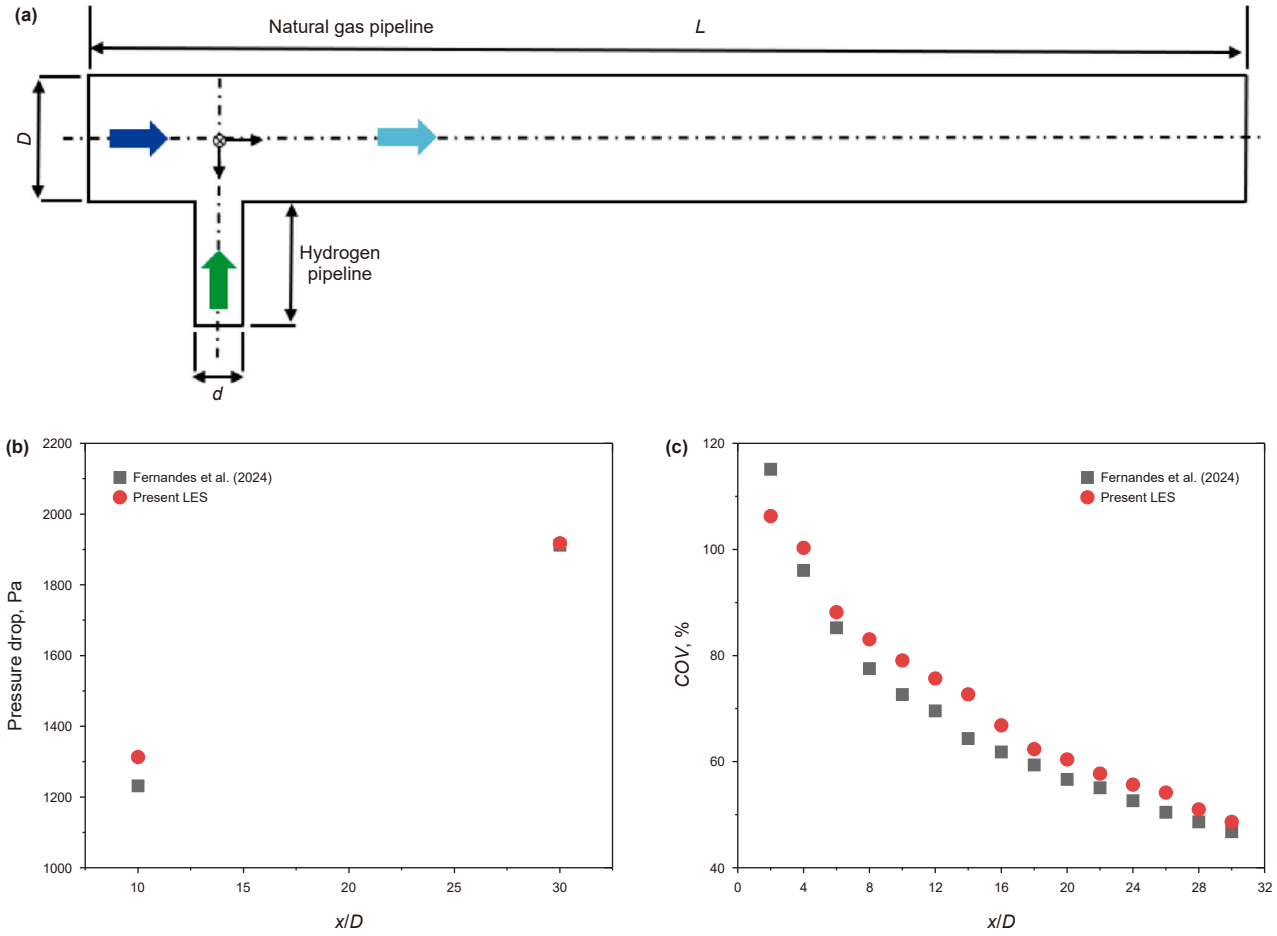

Fig. 2. The mixing results of a T-junction: **(a)** computational model (Su et al., 2022); **(b)** pressure drop; **(c)** *COV*.

0.9%. These results indicate that further refinement had a limited effect on the computational outcomes. Consequently, the mesh containing 1,969,124 cells was selected for subsequent simulations.

4. Results and discussion

4.1. Effect of orientation

Two stacking orientations, represented as Case 1 and Case 2 in Table 3, were examined to evaluate the effect of mixing element arrangement on the mixing performance. The mixing element shown in Fig. 1 is initially positioned horizontally and then rotated 90° to achieve a vertical orientation. As shown in Fig. 4(a), the *COV* values for the horizontal and vertical arrangements are nearly identical at positions where $x^*/D \leq 2$. However, within the range of $2 < x^*/D \leq 20$, the *COV* curve for the vertically arranged mixing elements drops rapidly before stabilizing, whereas that for the horizontal configuration declines more gradually. At $x^*/D = 20$, the *COV* value for the vertical arrangement is 2.59%, while that for the horizontal arrangement is 10.91%. Both cases exceed the homogeneity threshold, indicating that the gas mixture remains nonuniform. These suggest that a single mixing element is insufficient to achieve the desired level of homogeneity, and further optimization of the mixing element geometry or the inclusion of multiple mixing elements is necessary.

As illustrated in Fig. 5, the flow and mixing behaviors within the SMV static mixer can be divided into four distinct regions. In Region 1, prior to entering the mixing section, the hydrogen accumulates near the upper wall because of the density difference between the hydrogen and methane. Upon entering Region 2, the internal mixing elements redirect the flow, initiating interfacial interaction between the gases. The geometry-induced flow deflection in Region 2 causes divergent hydrogen trajectories, resulting in noticeable differences in spatial distribution in Region 3. In the horizontal configuration, the flow channels guide the hydrogen to flow downward, reducing its concentration near the top of the pipe. In contrast, in the vertical configuration, the hydrogen is directed toward the sidewalls and develops a helical axial flow that enhances the transverse mixing through increased radial mass transport. In Region 4, further downstream, the influence of the mixer gradually diminishes. The hydrogen distribution becomes increasingly homogeneous, and the mixing process is dominated by the turbulent diffusion, as indicated by the attenuation of concentration gradients and the absence of significant flow redirection.

Table 4 presents the pressure drop results corresponding to simulation cases listed in Table 3. These cases were designed according to the principle of controlled variables, in which only one geometric parameter was varied in each case while all others were held constant. The results show that, when the mixing elements are arranged horizontally, the pressure drop increases by 2.69% (Cases 1 and 2). Moreover, all simulated pressure drops in this study are significantly below the allowable limit of 0.2 MPa, according to the SY/T 5922-2024 “Specification for operation of gas pipelines”.

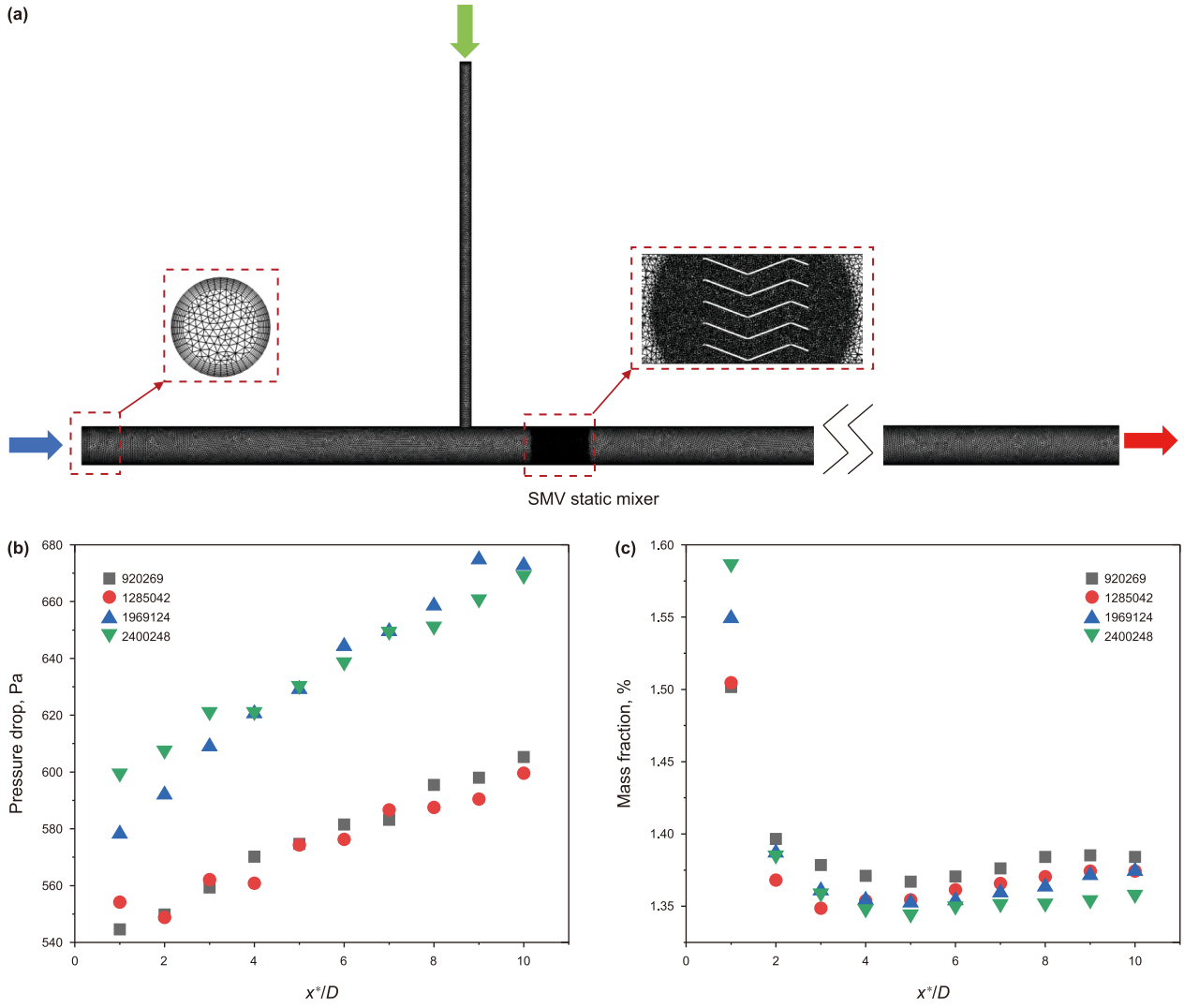

Fig. 3. Grid sensitivity analysis results: **(a)** computational domain mesh; **(b)** pressure drop; **(c)** mass fraction.

4.2. Effect of aspect ratio

As illustrated in Fig. 4(b), the variation of *COV* along the downstream direction is presented for different aspect ratios. None of the cases achieve complete homogeneity within $x^* = 20D$. No direct linear correlation is observed between the aspect ratio and *COV*. In the near-field region ($x^*/D \leq 8$), the curves corresponding to aspect ratios of 1.0 and 1.4 exhibit a rapid decrease in *COV*, whereas those for 1.2 and 1.6 show a gradual decline. In the far-field region ($x^*/D > 8$), all *COV* curves tend to level off as the turbulence decays and the flow becomes more stable. This suggests that the influence of the mixing element is strongest near the static mixer and progressively weakens downstream. As the fluid moves away from the mixer, the dissipation of the turbulence reduces the effect of the mixing structure on the flow field. At the final monitoring section, the *COV* values for aspect ratios of 1.0 and 1.4 are 2.59% and 2.03%, respectively, suggesting relatively superior mixing performance. As shown in Fig. 6, Region 3 plays a critical role in determining overall mixing performance. In particular, Fig. 6(b) reveals a pronounced accumulation of the hydrogen near the upper section of the pipeline within this region, indicating insufficient mixing. This spatial inhomogeneity aligns well with the *COV* results observed, further validating the quantitative assessment.

The mixing results for the two aspect ratios exhibit similar trends due to the shared structural characteristics of the corrugated plates. As shown in Fig. 1(c), all four aspect ratios feature identical inlet configuration, while their outlet structures differ from each other. For aspect ratios of 1.0 and 1.4, the outlets are located in the straight sections of the corrugated plates, whereas for aspect ratios of 1.2 and 1.6, the outlets are located within the twisted sections. These structural differences influence the downstream flow field, as illustrated in Fig. 6. Both the outlet structure and aspect ratio affect overall mixing performance, and only increasing the aspect ratio does not necessarily lead to improved mixing. Furthermore, the pressure drop (Table 4) is also influenced by the outlet configuration. Considering the trade-off between mixing performance and pressure drop, it is advisable to employ mixing elements with a standard aspect ratio. Therefore, the subsequent simulations, the aspect ratio was fixed at $L_e/D_e = 1.0$.

4.3. Effect of twist angle

The corrugated plate angle is a fundamental design parameter of the SMV static mixer and is critical to the mixing performance. In this study, four plate angles were selected for comparison: 45°, 60°, 90°, and 120°, corresponding to Cases 2, 6, 7, and 8 in Table 3,

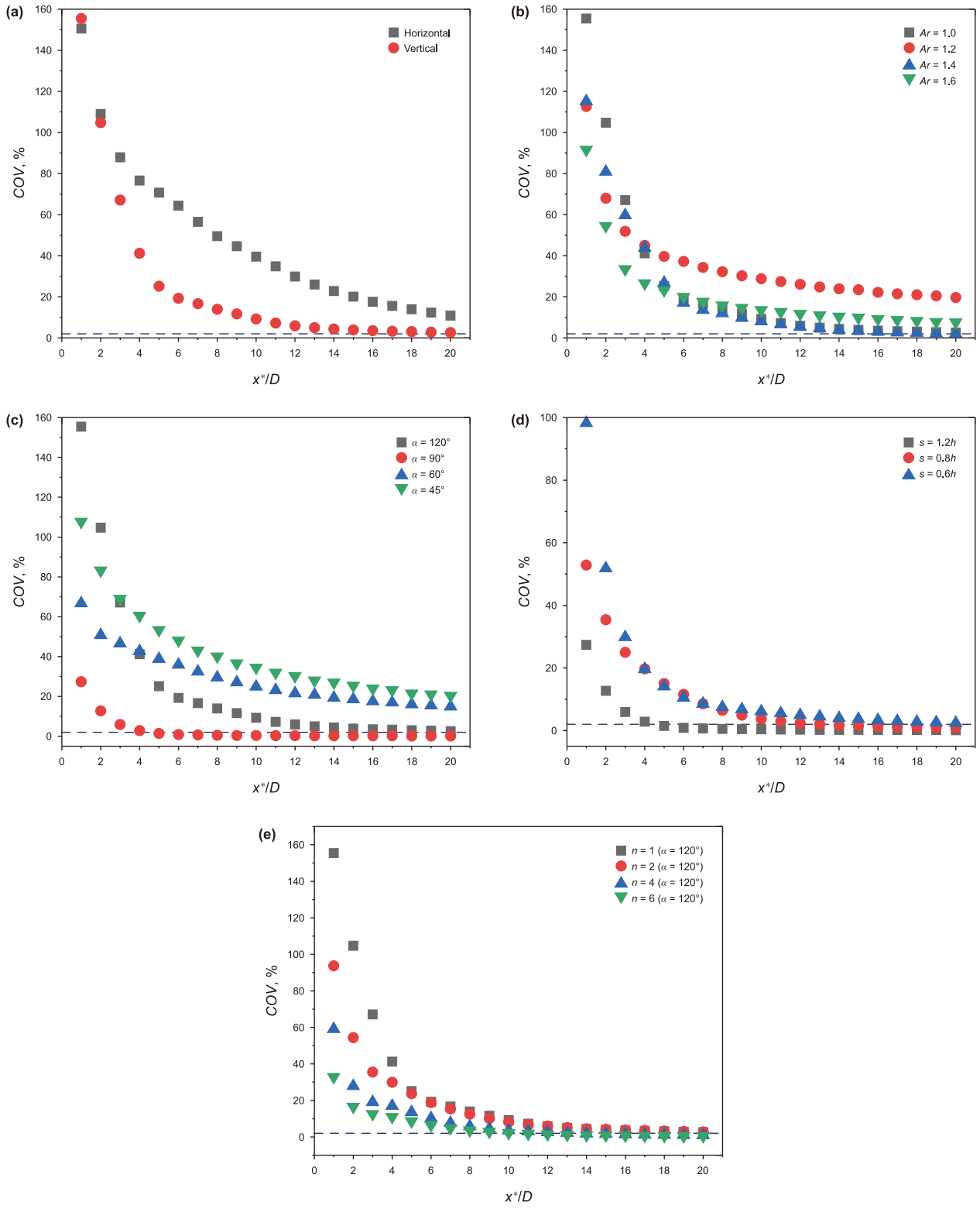

Fig. 4. *COV* evolution with distance: **(a)** orientation; **(b)** aspect ratio; **(c)** twist angle; **(d)** spacing height; **(e)** number of mixing elements.

respectively, to systematically evaluate the effect of plate angle variation on mixing efficiency and the associated pressure drop.

Fig. 4(c) shows that only the 90° configuration achieves mixing homogeneity at $x^*/D = 5$. The differences in the hydrogen distribution at various twist angles mainly attributed to the modified flow trajectories induced by the corrugated plate geometry. Changes in plate angle alter the curvature and orientation of the internal flow channels, which in turn affect the local centrifugal forces and generate secondary flows with varying strength and structure in both radial and circumferential directions. These

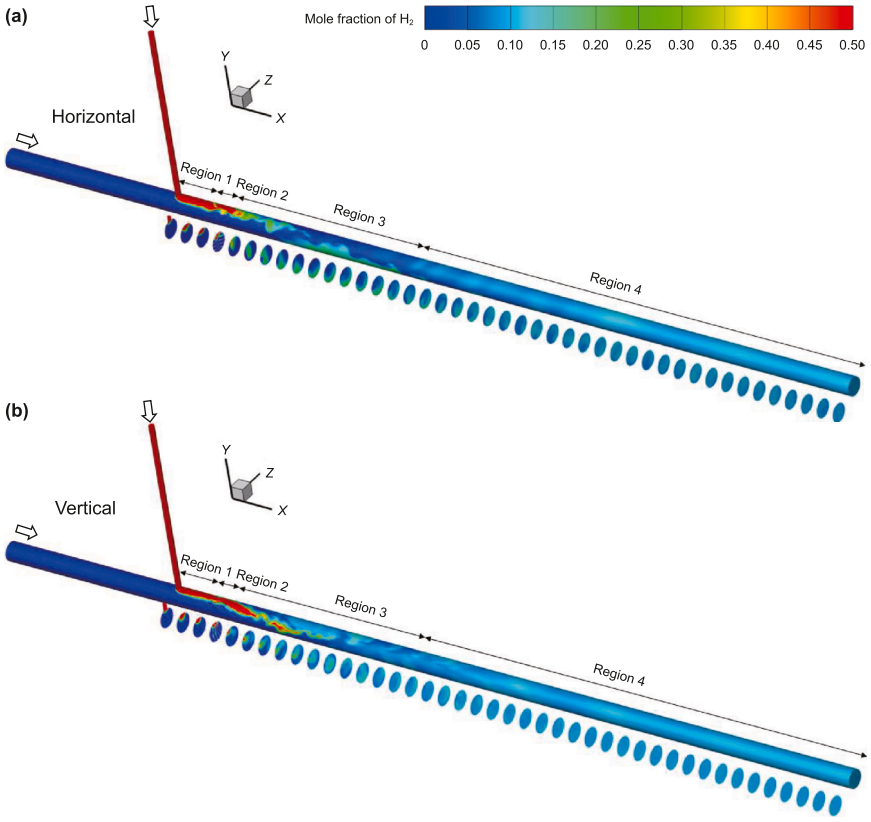

Fig. 5. Hydrogen mole fraction contours for different arrangement orientations.

secondary flows are intrinsically linked to the formation of vortex structures (Hong et al., 2024) and play a key role in mitigating stratification caused by the low density of hydrogen (Su et al., 2025). They facilitate the redistribution of hydrogen from the upper region of the pipe toward the central and lower areas, enhancing the radial mass transport and improving mixing homogeneity. The mechanisms of vortex formation and their impact on mixing behavior will be further discussed in the following section.

According to Fig. 7, at $\alpha = 120°$, a high-concentration hydrogen stream exits the mixer and travels through Regions 2 and 3, spiraling along the right wall of the pipeline toward the bottom. This produces the highest *COV* during the initial stage. At $\alpha = 90°$, the hydrogen current is redirected toward the left wall. Compared with $\alpha = 120°$, it has a lower concentration and disperses more rapidly, continuing to mix effectively in Region 3 and resulting in the best mixing performance. At $\alpha = 60°$, the hydrogen stream moves from the left to the right wall, undergoing partial mixing during this process; however, it persists throughout the Region 3. At $\alpha = 45°$, the hydrogen stream exits the static mixer along the left wall and flows downstream with a little change in concentration, indicating the poor mixing throughout this region. This unmixed hydrogen stream extends from the outlet of the static mixer to the midpoint of Region 4, which explains why the *COV* at 45° is higher than that at 60°. As summarized in Table 4, the pressure drop is highest at $\alpha = 90°$, followed by 60° and 45°, while the configuration with 120° exhibits the lowest pressure drop.

4.4. Effect of spacing height

The spacing height between the corrugated plates determines the number of layers within a single mixing element. A smaller spacing height corresponds to a larger number of plate layers. To investigate the effect of spacing height on mixing performance and pressure drop, three spacing configurations were examined: $s = 0.6h$, $0.8h$, and $1.2h$, corresponding to 9, 7, and 5 corrugated-plate layers (Cases 6, 9, and 10), respectively.

As shown in Fig. 8, under different corrugated-plate spacing heights, the hydrogen flow behavior in Regions 1 and 2 remains largely consistent. The flow mainly progresses in an orderly manner through the curved channels formed between the plates, accompanied by a moderate degree of shear disturbance. Unlike the variations in outlet flow direction caused by changes in installation orientation, aspect ratio, or twist angle, altering the spacing height primarily modifies the channel width without affecting the overall flow direction. As a result, the main flow continues to propagate along the sidewalls. However, the intensity

Table 4
Pressure drop results.

Case	1	2	3	4	5	6	7	8	9	10	11	12	13
ΔP, Pa	664.4	682.3	740.3	703.7	724.4	3674.9	1872.7	1322.7	3091.5	3247.3	1511.3	2924.1	4395.5

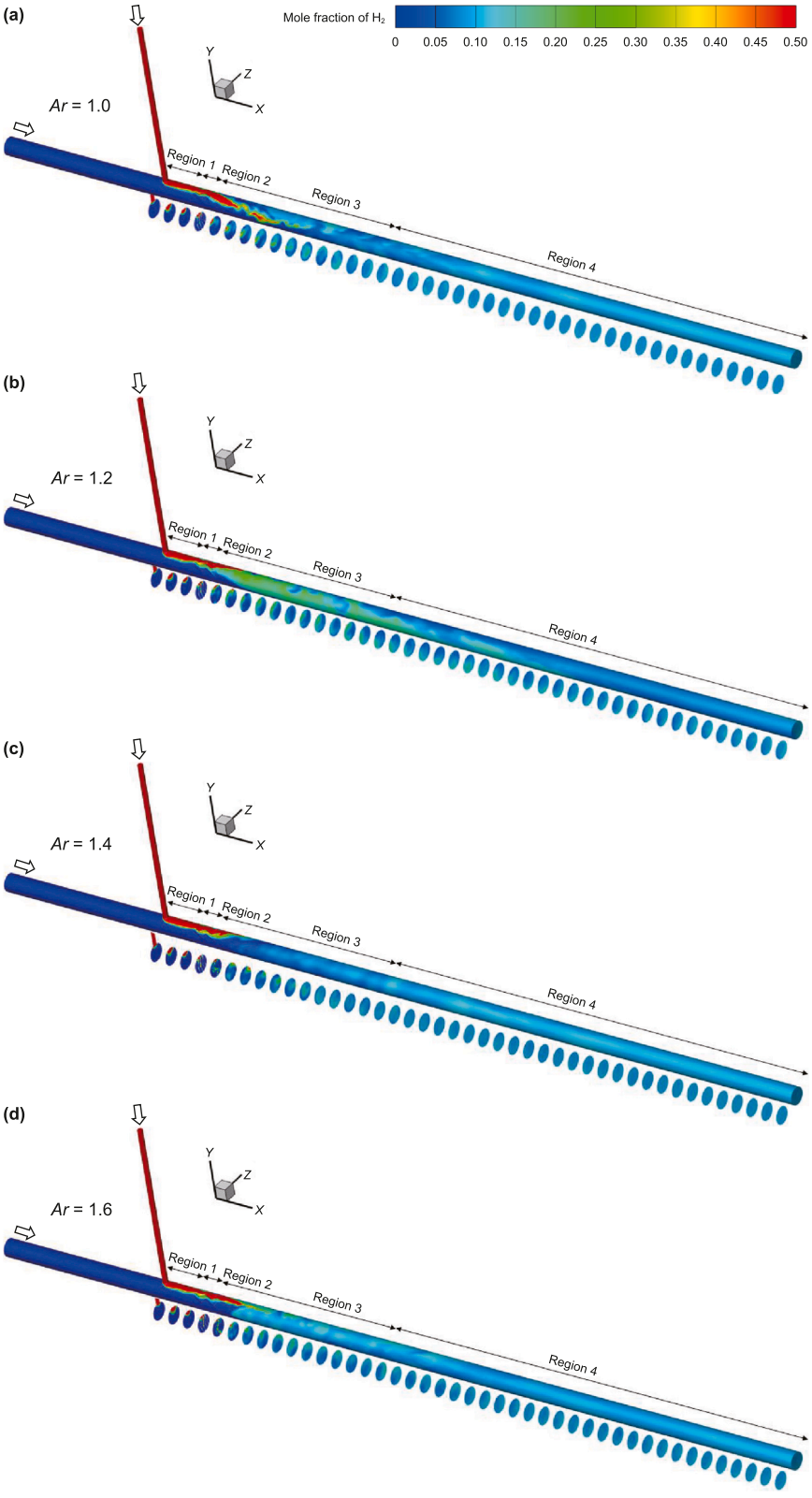

Fig. 6. Hydrogen mole fraction contours for different aspect ratios.

of the spiral development varies markedly along with spacing height, as reflected by the fluctuation amplitude of hydrogen concentration in Regions 3 and 4. Such spiral flow pattern is characterized by the distinct rotational motion and radial diffusion, manifesting as periodic concentration oscillations across the pipe cross-section. Structurally, it shares certain similarities with the spiral flow observed in conventional helical static mixers (Fernandes et al., 2024). In both cases, the mixer geometry induces

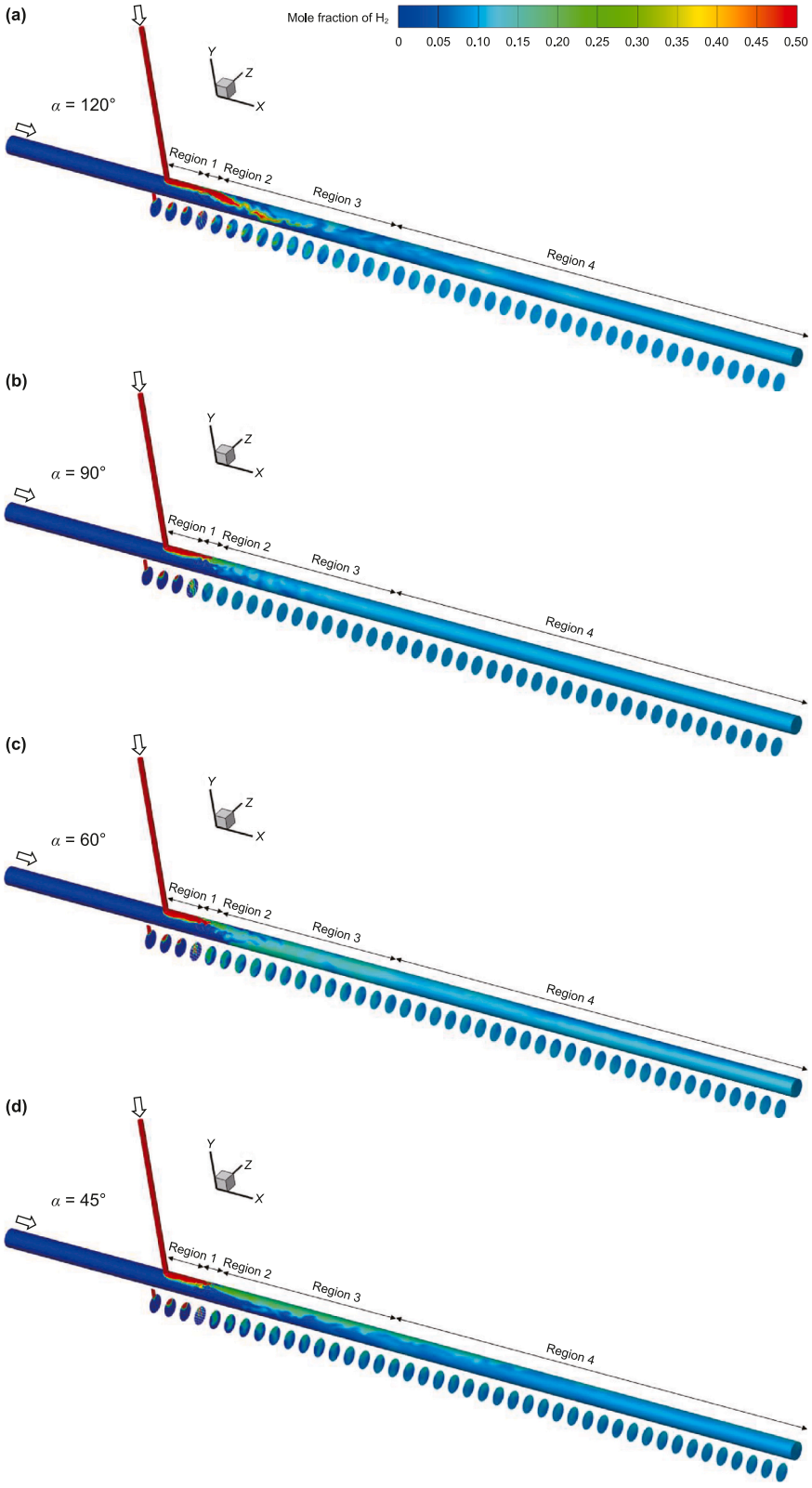

Fig. 7. Hydrogen mole fraction contours for different twist angles.

the rotational guidance and shear perturbations, generating secondary flow structures that disrupt stratification and enhance mixing efficiency. Nevertheless, the underlying mechanisms differ: the helical mixer relies on the alternating arrangement of helical blades to induce periodic flow inversion and cross-flow mixing (Zidouni et al., 2015), whereas the SMV static mixer forms the quasi-spiral flow through continuously curved channels created by the corrugated plates, promoting locally induced rotational and radial disturbances that naturally evolve into vortex structures.

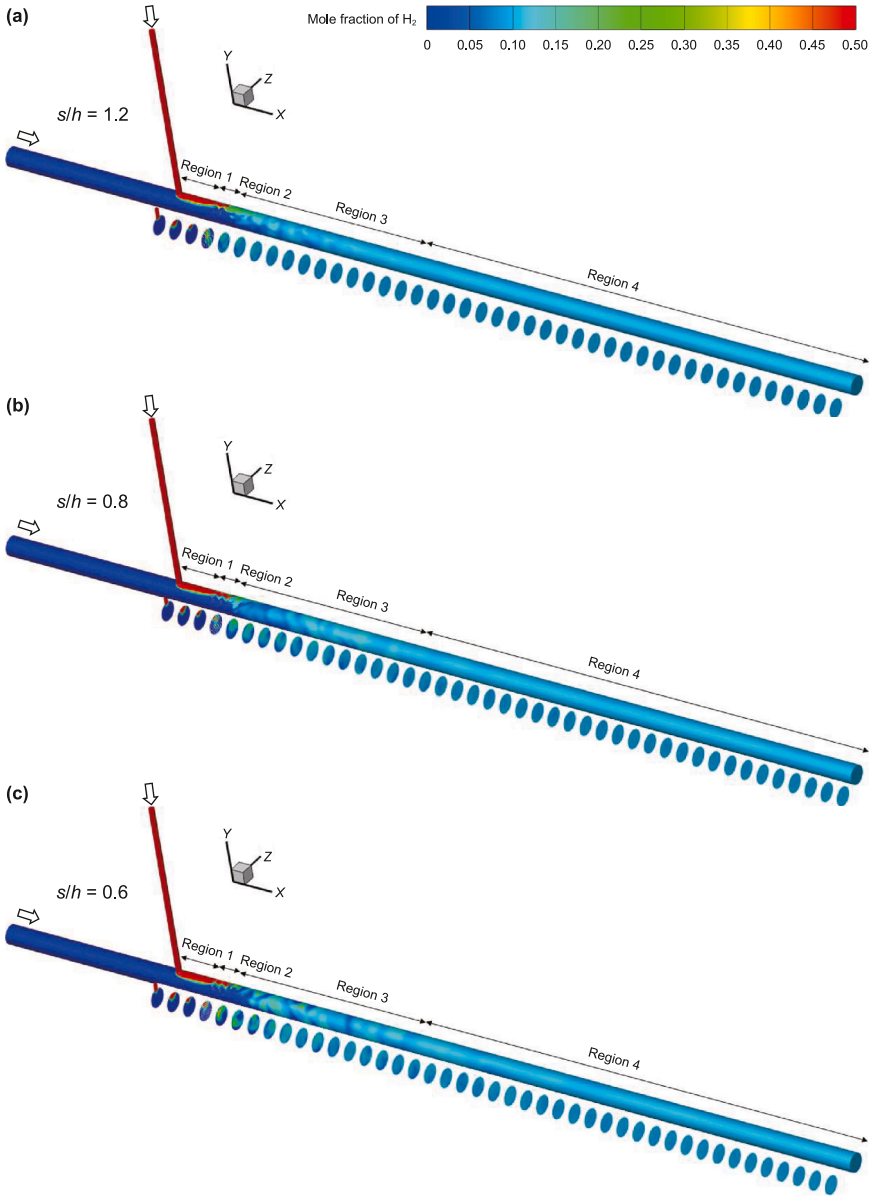

Fig. 8. Hydrogen mole fraction contours for different spacing heights.

A larger spacing height ($s = 1.2h$) creates a wider flow passage, which further enhances the rotational inertia and centrifugal forces as the fluid navigates the curved paths. This promotes the formation and persistence of strong vortices, enables hydrogen to detach more readily from the upper wall and entrain rapidly into the main flow, thereby accelerating radial diffusion and mixing. In contrast, a smaller height ($s = 0.6h$) restricts the rotational motion of the fluid, inhibits vortex development and weakens the spiral flow structure. Consequently, the hydrogen forms a distinct concentration lag zone in the downstream region. From the perspective of flow resistance, a reduced spacing height decreases the effective hydraulic diameter, increases local shear rates, and intensifies viscous dissipation. According to the Darcy–Weisbach equation, these effects lead to a notable increase in the pressure drop per unit length, which is consistent with the results shown in Table 4.

4.5. Effect of the number of mixing elements

The preceding analysis investigated the key structural parameters of the SMV static mixer, highlighting their effects on both of the mixing performance and pressure drop. Although the 90° configuration achieved homogeneous mixing, it produced an excessively high pressure drop. In contrast, the 120° configuration offered a better compromise between the mixing efficiency and the pressure drop. Building on these observations, this section explores the effect of increasing the number of mixing elements. The optimal baffle length and spacing were adopted from previous simulations. In the current setup, adjacent mixing elements are arranged in a staggered configuration, with the second, fourth, and sixth elements rotated by 90° relative to the first, third, and fifth (Ghanem et al., 2014; Abrofarakh, 2025).

As illustrated in Fig. 9, increasing the number of mixing elements extends Region 2, where the primary mixing occurs. When the number of elements is limited to one or two, a distinct hydrogen stream persists into Region 3. In contrast, with four or six elements, the hydrogen and methane undergo continuous intermixing within the static mixer, thereby eliminating well-defined hydrogen streams in Region 3. Due to the consistent outlet orientation of mixing elements, the hydrogen is directed

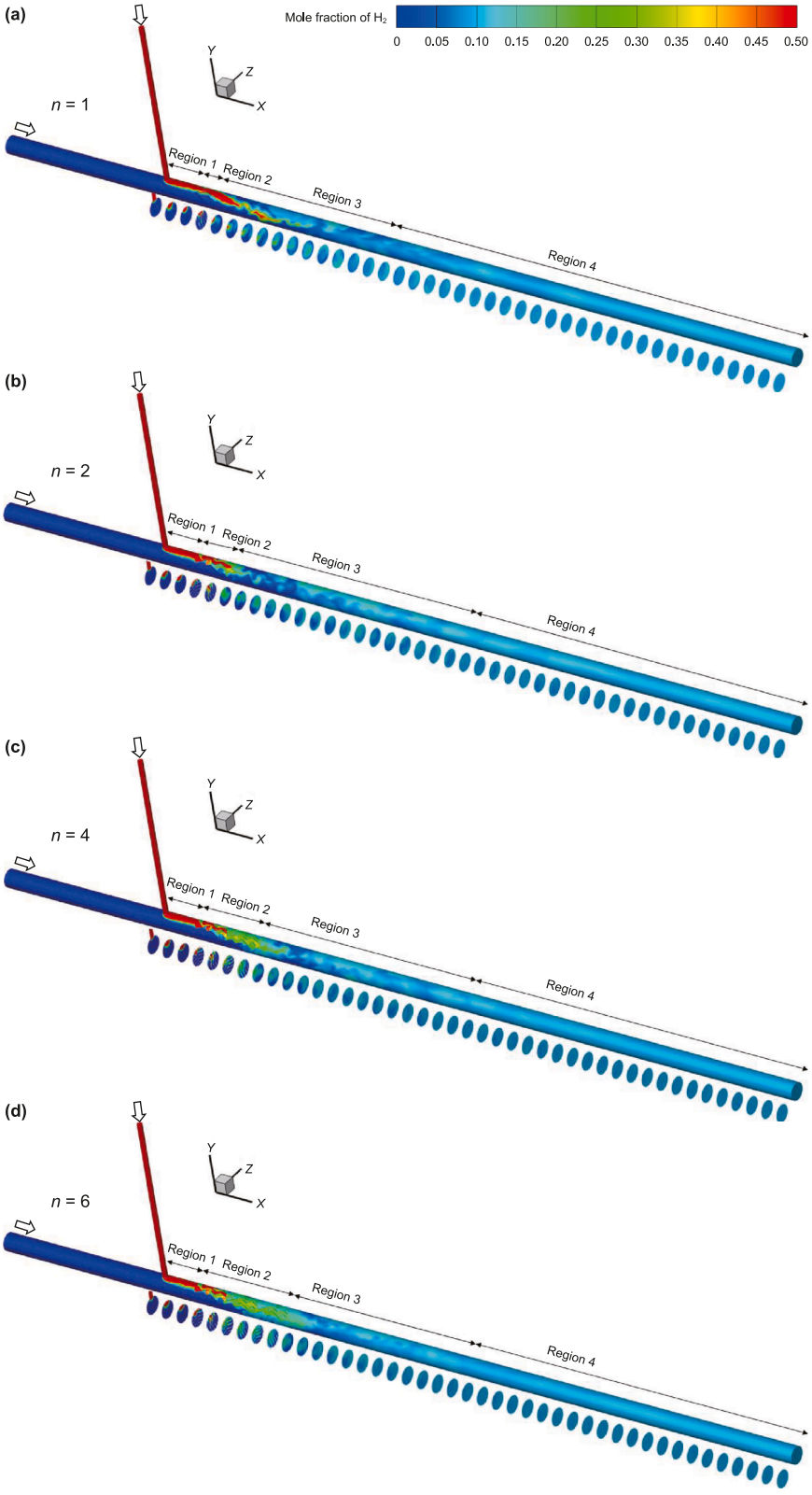

Fig. 9. Hydrogen mole fraction contours for different numbers of mixing elements.

toward the pipeline sidewalls at the outlet. As the number of mixing elements increases, the hydrogen mole fraction gradually decreases, and the fluid in downstream Regions 3 and 4 turns to more homogeneously mixed. This observation agrees well with the trend shown in Fig. 4(e). For cases with one or two elements, homogeneous mixture is not achieved even at $x^* = 20D$. However, configurations with four and six elements meet the mixing criterion at $x^* = 14D$ and $10D$, respectively. In the range of $x^*/D = 1$–5, the rate of *COV* reduction decreases as n increases, indicating diminishing returns with the addition of more elements. Meanwhile, Table 4 shows that the pressure drop increases with n, although the rate of increase gradually declines.

4.6. Flow and mixing characteristics

To elucidate the mixing characteristics of the methane and hydrogen and the corresponding pressure drop under different geometric parameters, the vortex evolution and flow-field characteristics were further examined to reveal the underlying mixing mechanisms of the SMV static mixer.

Fig. 10 illustrates the velocity fields and vortex structures at multiple cross-sections within the SMV static mixer (L^*/L_e) and in the immediate downstream region (x^*/D = 1–3), showing the evolution of flow characteristics as the fluid traverses the mixer. As shown in the first column, the inlet streamlines appear similar across all mixer configurations, with the high-velocity flow concentrated near the channel centerline. However, distinct variations in the velocity distribution develop downstream, driven by differences in flow-channel geometry, which in turn exert a significant influence on both mixing efficiency and pressure drop.

As seen in Fig. 10(a) and (b), low-velocity zones appear between the corrugated plates and the pipe wall. In Fig. 10(b), the improved fluid distribution mitigates hydrogen accumulation in the upper region by alleviating localized stagnation. The vortex structures differ notably between the two configurations. In the horizontal layout, a pair of horizontally symmetric vortices of unequal size emerges at the $x^*/D = 1$ cross-section, whereas the vertical layout produces four vortices of varying sizes. As the flow progresses downstream, smaller vortices gradually merge into larger coherent structures, consistent with the findings of Chakleh and Azizi (2023). Eventually, a pair of symmetric, counter-rotating vortices forms in the upper and lower parts of the channel. These structures, known as Dean vortices, are induced by the curved and twisted flow paths created by the corrugated plates (Ben Haroual et al., 2025). Dean vortices develop when centrifugal forces act on fluid layers moving through curved passages, generating transverse swirling motion superimposed on the primary axial flow (Peng et al., 2022; Pinho et al., 2023). These secondary flows intensify radial convection by transporting fluid alternately between the pipe center and wall, thereby enhancing cross-sectional mass transfer and promoting rapid mixing homogeneity. This effect is evident in the observed reduction of *COV*. However, the turbulence and flow disturbances associated with Dean vortices also increase the viscous dissipation, leading to a higher pressure drop across the static mixer, as summarized in Table 4.

As shown in Fig. 10(b), (c), (d), and (e), comparative analyses of the flow-field structures at different aspect ratios reveal that the downstream flow patterns for $Ar = 1$ and 1.4, as well as for $Ar = 1.2$ and 1.6, exhibit similar characteristics, mainly due to their comparable outlet configurations. For $Ar = 1$ and 1.4, the vortices are vertically symmetric, and the larger aspect ratio enhances longitudinal shear effects, resulting in stronger vortex activity and intensified shear forces that improve mixing. However, for $Ar = 1.2$ and 1.6, the formation of four symmetrically distributed vortices gives rise to a more complex vortex system. Although the number of vortices increases, the interactions among them remain weak, and the limited coupling between shear forces and vortex motion slows turbulent energy dissipation, thereby reducing mixing efficiency. Notably, the vortex structure at $Ar = 1.2$ evolves most slowly and exhibits the weakest vortex interactions, which explains its relatively poor mixing performance. Furthermore, variations in the flow-field structure associated with the outlet positions of the mixing elements represent a key factor contributing to pressure-drop fluctuations.

As seen in Fig. 10(b), (f), (g), and (h), smaller twist angles (45° and 60°) force the fluid to pass through narrower and more curved flow paths, resulting in pronounced streamline deflection and strong velocity gradients near the plate surfaces. These conditions generate small-scale, near-wall vertical vortices with lower energy, limited spatial development, and weaker radial penetration, rendering them ineffective at disrupting the main flow. Consequently, low-velocity zones and localized hydrogen accumulation appear downstream. At 90°, the flow undergoes significant directional changes, producing high shear and centrifugal effects that induce a broad spectrum of vortex structures. These include both near-wall vortices and large spiral vortices extending across the pipe cross-section. Such structures significantly enhance momentum and mass transfer, thereby improving mixing efficiency. In the 120° configuration, the flow experiences relatively mild deflection, leading to reduced local shear and weaker centrifugal forces. As a result, vortex generation is less intense than in the 90° case, and the mixing enhancement effect is correspondingly diminished. Notably, the pressure drop does not exhibit a linear relationship with the twist angle. This observation suggests that energy loss in the SMV static mixer depends not only on the geometric features of the flow channels but also, more critically, on internal flow dynamics such as vortex-induced shear, turbulence generation, and viscous dissipation. The 120° configuration produces smoother flow with fewer disturbances, resulting in the lowest pressure drop, whereas the 90° configuration causes strong streamline curvature and vigorous vortex interactions, increasing shear and turbulence intensity and producing the highest pressure drop. Although smaller twist angles intensify flow tortuosity and local shear, the associated pressure drop remains moderate because the flow lacks strong vortex structures and effective momentum exchange.

As shown in Fig. 10(f), (i), and (j), reducing the spacing height narrows the flow channel and restricts the formation and strength of downstream vortices. Although certain vortex structures persist, their intensity is often insufficient to counteract adverse effects such as the flow separation or stagnant zones, thereby diminishing the mixing performance. The pressure drop does not vary linearly along with the spacing height, as it is governed jointly by the channel geometry and vortex dynamics. At $s = 1.2h$, the wider channel facilitates the generation of more complex vortices, resulting in higher local velocities and significant energy dissipation, which produce the largest pressure drop. At $s = 0.8h$, the vortex formation is limited, energy loss is reduced, and pressure drop decreases accordingly. However, at $s = 0.6h$, although vortex activity is minimal, the extremely narrow channel induces localized velocity peaks and increased frictional resistance, leading to a rebound in pressure drop.

As shown in Fig. 10(b), (k), (l), and (m), the inlet flow remains relatively simple, but as the number of mixing elements increases, the internal flow path becomes progressively more complex. Streamlines exhibit sharper curvature, and turbulence intensifies, particularly in the regions between adjacent elements. The vortex structures evolve into increasingly intricate, multiscale patterns that enhance the mass transport and mixing efficiency. With a

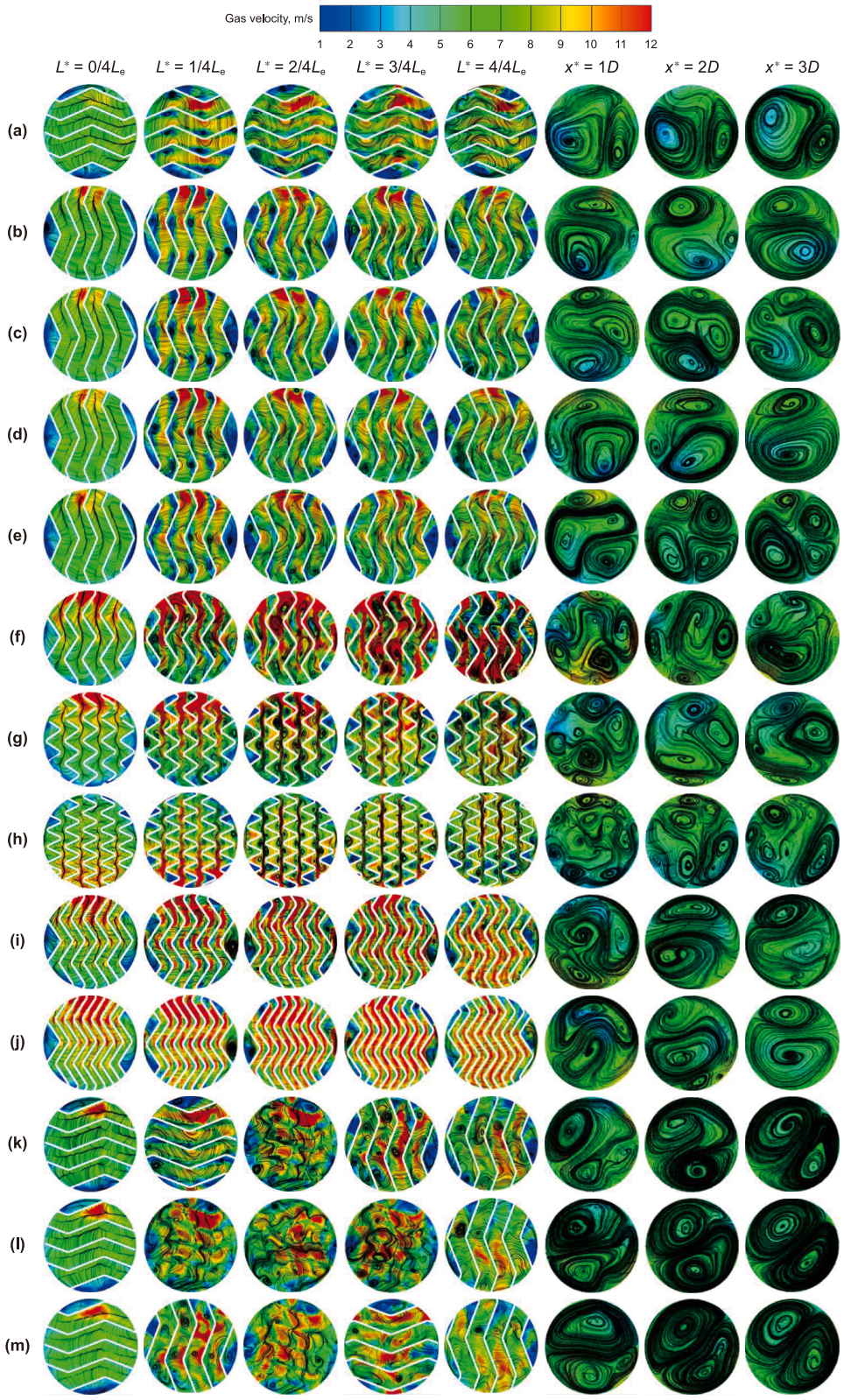

Fig. 10. Flow velocity contours and vortex evolution patterns for different SMV static mixer structures: **(a)** horizontal; **(b)** vertical; **(c)** $Ar = 1.2$; **(d)** $Ar = 1.4$; **(e)** $Ar = 1.6$; **(f)** $\alpha = 90°$; **(g)** $\alpha = 60°$; **(h)** $\alpha = 45°$; **(i)** $s/h = 0.8$; **(j)** $s/h = 0.6$; **(k)** $n = 2$; **(l)** $n = 4$; **(m)** $n = 6$.

further increase in the element count, the downstream flow field gradually stabilizes and vortex patterns converge, indicating that the system approaches a quasi-steady dynamic equilibrium. Although the mixing efficiency continues to improve, the rate of improvement diminishes, as shown in Fig. 9. Meanwhile, the pressure drop increases substantially with the addition of more elements. Initially, this rise is rapid due to strong flow disturbances, but the rate of increase slows as additional elements are incorporated (Table 4).

The vortex formation and evolution play a pivotal role in the mixing process. In the SMV static mixer, vortices are primarily generated by the curved and twisted flow channels, which induce shear-layer separation and secondary flow structures. These vortices intensify the local turbulence and promote hydrogen–methane interaction through shear deformation and vortex stretching. Serving as carriers of energy and momentum, they facilitate radial transport, diminish concentration gradients, and accelerate the homogenization. However, the increased turbulence also enhances the viscous dissipation, leading to a higher pressure drop across the mixer.

5. Conclusions

A systematic numerical study was conducted to investigate the influence of geometric variations of the SMV static mixer on the gas mixing and pressure drop features, with particular focus on the flow behavior of hydrogen and methane and the role of vortex evolution in the mixing process. The main conclusions are summarized as follows.

(1) The vertical SMV static mixer effectively suppresses low-velocity zones near the upper pipe wall, thereby preventing the hydrogen accumulation. With identical inlet and outlet structures, increasing the aspect ratio further enhances the mixing homogeneity. The 90° configuration generates multiscale vortex structures that yield the shortest mixing length but the highest pressure drop. In contrast, the 120° configuration produces the lowest pressure drop while maintaining a homogeneity second only to the 90°. Both the pressure drop and mixing efficiency increase along with the interlayer spacing, and the optimal design is five layers. At 120°, increasing the number of the mixing elements from one to six shortens the mixing length by approximately 2.5 times, whereas the pressure drop rises by a factor of 4.5.

(2) The SMV static mixer forms a distinctive internal flow structure characterized by a multiscale vortex system arising from the combined influence of geometric disturbances and intrinsic flow instabilities within the primary spiral motion. These vortices continuously evolve through mechanisms of formation, deformation, and interaction across wide spatial and temporal scales. Unlike the relatively stable helical flows in conventional helical mixers, the SMV mixer exhibits a highly unsteady flow field dominated by dynamic vortex interactions. Consequently, the pressure drop is governed not only by geometric parameters but also by the evolving complexity of the internal flow.

(3) Vortices enhance mixing through the fluid entrainment, vortex stretching, and turbulent diffusion. Large-scale vortices promote momentum exchange between primary and secondary flows, expanding the effective mixing region and strengthening the mass transfer. Small-scale vortices concentrated near the boundary layer help diminish local concentration gradients. Among the large-scale structures, geometry-induced Dean vortices are particularly important in SMV static mixer, as they intensify interlayer shear and generate secondary flow recirculation, and accelerates the mixing process. Unfortunately, these vortices also increase the energy dissipation. Therefore, controlling vortex dynamics and optimizing turbulent energy distribution are essential to designing efficient and low-resistance mixing systems.

CRediT authorship contribution statement

Tao Di: Writing – original draft, Validation, Software, Methodology, Investigation, Data curation. **Xu Sun:** Writing – review & editing, Supervision, Methodology. **Peng-Chao Chen:** Writing – review & editing, Software, Conceptualization. **Hong-Yu Zhou:** Validation, Data curation. **Qi-Yu Huang:** Investigation. **Xiao-Ben Liu:** Visualization.

Declaration of competing interest

The authors declare that they have no known competing financial interests or personal relationships that could have appeared to influence the work reported in this paper.

References

Abrofarakh, M., 2025. Effect of incorporating sulzer SMV static mixers on the performance of direct contact membrane distillation (DCMD): A three-dimensional computational fluid dynamics (CFD) study. Sep. Purif. Technol. 359, 130606. https://doi.org/10.1016/j.seppur.2024.130606.

Albertazzi, J., Busini, V., Rota, R., 2024. Comparison through a CFD approach of static mixers in an emulsification process. Int. J. Thermofluids 22, 100708. https://doi.org/10.1016/j.ijft.2024.100708.

Ali, N., Tormene, F., 2025. An innovative method for blending hydrogen into natural gas. Int. J. Hydrogen Energy 148, 150038. https://doi.org/10.1016/j.ijhydene.2025.150038.

An, Y.W., Jia, G.W., Xu, W.Q., et al., 2023. Performance analysis of multiple structural parameters of injectors for hydrogen-mixed natural gas using orthogonal experimental methods. Phys. Fluids 35 (11), 117119. https://doi.org/10.1063/5.0175018.

Ben Haroual, B., Albagnac, J., Brancher, P., et al., 2025. Experimental investigation of dean-vortices oscillation downstream of a 90° bend. Exp. Therm. Fluid Sci. 163, 111402. https://doi.org/10.1016/j.expthermflusci.2024.111402.

Bennour, E., Kezrane, C., Kaid, N., et al., 2023. Improving mixing efficiency in laminar-flow static mixers with baffle inserts and vortex generators: A three-dimensional numerical investigation using corrugated tubes. Chem. Eng. Process. Process Intensif. 193, 109530. https://doi.org/10.1016/j.cep.2023.109530.

Bie, H.Y., Liu, J.H., Xue, L.C., et al., 2025. Flow mechanism and mixing enhancement in a micromixer based on trigonometric baffles. Chem. Eng. Sci. 316, 121970. https://doi.org/10.1016/j.ces.2025.121970.

Casugbo, C., Baker, M.R., 2018. Pumping capacity of inline dynamic mixers and its effect on process flow control. Chem. Eng. Res. Des. 132, 982–988. https://doi.org/10.1016/j.cherd.2018.02.005.

Chakleh, R., Azizi, F., 2023. Performance comparison between novel and commercial static mixers under turbulent conditions. Chem. Eng. Process. Process Intensif. 193, 109559. https://doi.org/10.1016/j.cep.2023.109559.

Chen, X.R., Wang, H., Wang, X.Y., et al., 2023. Fuel/air mixing characteristics of a micromix burner for hydrogen-rich gas turbine. Energy 282, 128786. https://doi.org/10.1016/j.energy.2023.128786.

Chen, Y.B., Bao, R.X., Li, J., et al., 2025. Evaluation of the impact of hydrogen blending on the process characteristics of a cold energy power generation system. J. Clean. Prod. 499, 145235. https://doi.org/10.1016/j.jclepro.2025.145235.

Delaplace, G., Xiao, J., Buendia, F., et al., 2023. Framework for choosing energy efficient mixing equipment whatever motions it induces: Example of application for planetary and helical ribbon mixers. Chem. Eng. Res. Des. 198, 173–183. https://doi.org/10.1016/j.cherd.2023.08.042.

Di, T., Sun, X., Chen, P.C., et al., 2024. A novel static mixer for blending hydrogen into natural gas pipelines. Int. J. Hydrogen Energy 86, 1118–1128. https://doi.org/10.1016/j.ijhydene.2024.08.494.

Eames, I., Austin, M., Wojcik, A., 2022. Injection of gaseous hydrogen into a natural gas pipeline. Int. J. Hydrogen Energy 47 (61), 25745–25754. https://doi.org/10.1016/j.ijhydene.2022.05.300.

Etchells Iii, A.W., Meyer, C.F., 2003. Mixing in Pipelines. Handbook of Industrial Mixing: Science and Practice, pp. 391–477. https://doi.org/10.1002/0471451452.ch7.

Fernandes, L.A., Marcon, L.R.C., Rouboa, A., 2024. Simulation of flow conditions for natural gas and hydrogen blends in the distribution natural gas network. Int. J. Hydrogen Energy 59, 199–213. https://doi.org/10.1016/j.ijhydene.2024.01.014.
Gao, X.F., Tang, M., Wang, D.W., et al., 2024. The effect of periodic spatial arrangement of rotational–perforated static mixer on chaotic advection behavior. Chem. Eng. Sci. 292, 119917. https://doi.org/10.1016/j.ces.2024.119917.
Gao, Z.W., Liu, Z.X., Wei, Y.D., et al., 2022. Numerical analysis on the influence of vortex motion in a reverse stairmand cyclone separator by using LES model. Pet. Sci. 19 (2), 848–860. https://doi.org/10.1016/j.petsci.2021.11.009.
Ghanem, A., Lemenand, T., Della Valle, D., et al., 2014. Static mixers: Mechanisms, applications, and characterization methods – A review. Chem. Eng. Res. Des. 92 (2), 205–228. https://doi.org/10.1016/j.cherd.2013.07.013.
Guo, W.W., Jiang, Z.L., Zhong, H.H., et al., 2023. Impact of online mixing via KSM on the accuracy of ingredient deposition in manufacturing FGMs. Int. J. Mech. Sci. 241, 107971. https://doi.org/10.1016/j.ijmecsci.2022.107971.
Hong, H., Doh, I., Jeong, J., et al., 2024. Mixing enhancement with generation of effective secondary flow parallel to fluid interface in three-dimensional serpentine channel. Results Eng. 24, 103362. https://doi.org/10.1016/j.rineng.2024.103362.
Hoque, M.A., Mallik, M.S.I., Hossain, M.S., et al., 2024. Large eddy simulation of a turbulent channel flow using dynamic smagorinsky subgrid scale model and differential equation wall model. Int. J. Thermofluids 22, 100676. https://doi.org/10.1016/j.ijft.2024.100676.
Horie, T., Nakatsune, K., Matsumoto, T., et al., 2011. Liquid–liquid two phase flow of millichannel with a dynamic mixer. Chem. Eng. Process. Process Intensif. 50 (1), 1–8. https://doi.org/10.1016/j.cep.2010.10.007.
Ichikawa, Y., 2024. Retrofit concept for 100% hydrogen operation on natural gas lean-burn engine with spark ignition and prechamber system: Engine performance under hydrogen-mixing and load limits. Int. J. Hydrogen Energy 60, 1275–1287. https://doi.org/10.1016/j.ijhydene.2024.02.159.
Jia, G.W., Lei, M.Y., Li, M.Y., et al., 2023. Hydrogen embrittlement in hydrogen-blended natural gas transportation systems: A review. Int. J. Hydrogen Energy 48 (82), 32137–32157. https://doi.org/10.1016/j.ijhydene.2023.04.266.
Khabbazi, A.J., Zabihi, M., Li, R., et al., 2024. Mixing hydrogen into natural gas distribution pipeline system through tee junctions. Int. J. Hydrogen Energy 49, 1332–1344. https://doi.org/10.1016/j.ijhydene.2023.11.038.
Kong, M.M., Feng, S.M., Xia, Q., et al., 2021. Investigation of mixing behavior of hydrogen blended to natural gas in gas network. Sustainability 13 (8), 4255. https://doi.org/10.3390/su13084255.
Kouadri, A., Douroum, E., Lasbet, Y., et al., 2021. Comparative study of mixing behaviors using non-newtonian fluid flows in passive micromixers. Int. J. Mech. Sci. 201, 106472. https://doi.org/10.1016/j.ijmecsci.2021.106472.
Liu, C.W., Pei, Y.B., Cui, Z.X., et al., 2023a. Study on the stratification of the blended gas in the pipeline with hydrogen into natural gas. Int. J. Hydrogen Energy 48 (13), 5186–5196. https://doi.org/10.1016/j.ijhydene.2022.11.074.
Liu, G.X., Li, L., Jia, B., 2025. Mixing characteristics of kerosene with different equivalence ratios at different pulse frequencies in a supersonic combustor. Fuel 387, 134408. https://doi.org/10.1016/j.fuel.2025.134408.
Liu, Q., Liu, Y., Li, S.J., et al., 2022. Analysis of the static mixer effect on natural gas mixing process in a pipeline. Flow Meas. Instrum. 85, 102146. https://doi.org/10.1016/j.flowmeasinst.2022.102146.
Liu, S.Y., Liu, C., 2024. Scalar transport after a high-resolution solitary fractal tree based on large-eddy simulation: Implication to urban green infrastructure. J. Clean. Prod. 461, 142693. https://doi.org/10.1016/j.jclepro.2024.142693.
Liu, Y.Z., Rao, A., Ma, F.H., et al., 2023b. Investigation on mixing characteristics of hydrogen and natural gas fuel based on SMX static mixer. Chem. Eng. Res. Des. 197, 738–749. https://doi.org/10.1016/j.cherd.2023.07.040.
Lu, H.F., Xi, D.M., Cheng, Y.F., 2025. Hydrogen production in integration with CCUS: A realistic strategy towards net zero. Energy 315, 134398. https://doi.org/10.1016/j.energy.2025.134398.
Mirfasihi, S., Basu, W., Martin, P., et al., 2025. A numerical study on the mixing time prediction of miscible liquids with high viscosity ratios in turbulently stirred vessels. Chem. Eng. Sci. 304, 120944. https://doi.org/10.1016/j.ces.2024.120944.
Ouyang, X., He, Q., Chai, C., et al., 2024. A numerical study on hydrogen blending in natural gas pipeline by a T-pipe. J. Pipeline Sci. Eng. 4 (4), 100186. https://doi.org/10.1016/j.jpse.2024.100186.
Paglianti, A., Montante, G., 2013. A mechanistic model for pressure drops in corrugated plates static mixers. Chem. Eng. Sci. 97, 376–384. https://doi.org/10.1016/j.ces.2013.04.042.
Peng, K.L., Xu, F.S., Yang, L.X., et al., 2022. Dean instability and vortex-induced mixing for two miscible fluids in T-micromixers. Chem. Eng. Process. Process Intensif. 176, 108975. https://doi.org/10.1016/j.cep.2022.108975.
Pinho, B., Williams, L.M., Mahin, J., et al., 2023. Enhancing mixing efficiency in curved channels: A 3D study of bi-phasic dean-taylor flow with high spatial and temporal resolution. Chem. Eng. J. 471, 144342. https://doi.org/10.1016/j.cej.2023.144342.
Rabha, S., Schubert, M., Grugel, F., et al., 2015. Visualization and quantitative analysis of dispersive mixing by a helical static mixer in upward co-current gas–liquid flow. Chem. Eng. J. 262, 527–540. https://doi.org/10.1016/j.cej.2014.09.019.
Rosa, N., Azimi Fereidani, N., Cardoso, B.J., et al., 2025. Advances in hydrogen blending and injection in natural gas networks: A review. Int. J. Hydrogen Energy 105, 367–381. https://doi.org/10.1016/j.ijhydene.2025.01.314.
Ruan, D., Cheng, Y.Q., Hou, J.J., et al., 2024. Mass transfer and mixing performance in jet-to-counterflow micromixer. Chem. Eng. J. 498, 155348. https://doi.org/10.1016/j.cej.2024.155348.
Schrimpf, M., Esteban, J., Rösler, T., et al., 2019. Intensified reactors for gas-liquid-liquid multiphase catalysis: from chemistry to engineering. Chem. Eng. J. 372, 917–939. https://doi.org/10.1016/j.cej.2019.03.133.
Shi, L., Meng, X.B., Wu, Y., 2023. Numerical study on the propagation of CH_4/H_2 flame in a pipeline under different H_2 enrichment conditions. J. Clean. Prod. 423, 138689. https://doi.org/10.1016/j.jclepro.2023.138689.
Shi, Z.F., Jessen, K., Tsotsis, T.T., 2020. Impacts of the subsurface storage of natural gas and hydrogen mixtures. Int. J. Hydrogen Energy 45 (15), 8757–8773. https://doi.org/10.1016/j.ijhydene.2020.01.044.
Su, Y., Li, J.F., Guo, W.Y., et al., 2022. Prediction of mixing uniformity of hydrogen injection in natural gas pipeline based on a deep learning model. Energies 15 (22), 8694. https://doi.org/10.3390/en15228694.
Su, Y., Li, J.F., Yu, B., et al., 2023. Simulation study on the mixing of hydrogen and natural gas in static mixers. Nat. Gas. Ind. 43 (3), 113–122. https://doi.org/10.3787/j.issn.1000-0976.2023.03.012.
Su, Y., Li, J.F., Yu, B., et al., 2025. Study of hydrogen stratification phenomena in hydrogen-blended natural gas pipelines. Renew. Energy 253, 123603. https://doi.org/10.1016/j.renene.2025.123603.
Valdés, J.P., Kahouadji, L., Matar, O.K., 2022. Current advances in liquid–liquid mixing in static mixers: A review. Chem. Eng. Res. Des. 177, 694–731. https://doi.org/10.1016/j.cherd.2021.11.016.
Vashisth, V., Nigam, K.D.P., Kumar, V., 2021. Design and development of high shear mixers: Fundamentals, applications and recent progress. Chem. Eng. Sci. 232, 116296. https://doi.org/10.1016/j.ces.2020.116296.
Wang, J.X., Hao, X.Y., Zhang, H., et al., 2025. Simulation and experimental investigation on the static mixer of natural gas mixed with hydrogen. Int. J. Hydrogen Energy 99, 1–14. https://doi.org/10.1016/j.ijhydene.2024.12.045.
Wu, L., Hou, Z.M., Luo, Z.F., et al., 2024a. Impacts of microbial interactions on underground hydrogen storage in porous media: A comprehensive review of experimental, numerical, and field studies. Pet. Sci. 21 (6), 4067–4099. https://doi.org/10.1016/j.petsci.2024.08.015.
Wu, Z., Wang, C., Lang, R., et al., 2024b. The distribution of components in hydrogen-blended pipelines under different gas stream injection pattern. Fuel 375, 132577. https://doi.org/10.1016/j.fuel.2024.132577.
Yan, S.J., Jia, G.W., Xu, W.Q., et al., 2023. Computational fluid dynamic analysis of hydrogen–injected natural gas for mixing and transportation behaviors in pipeline structures. Energy Sci. Eng. 11 (8), 2912–2928. https://doi.org/10.1002/ese3.1500.
Yang, D.H., Sun, Y.Q., Tian, L., et al., 2024a. Investigation of the mixing characteristics of hydrogen and natural gas in different static mixers. Int. J. Hydrogen Energy 72, 166–178. https://doi.org/10.1016/j.ijhydene.2024.05.330.
Yang, L.X., Xu, F.S., Chen, G.W., 2024b. Effective mixing in a passive oscillating micromixer with impinging jets. Chem. Eng. J. 489, 151329. https://doi.org/10.1016/j.cej.2024.151329.
Zhang, C.G., Ferrell, A.R., Nandakumar, K., 2019. Study of a toroidal-helical pipe as an innovative static mixer in laminar flows. Chem. Eng. J. 359, 446–458. https://doi.org/10.1016/j.cej.2018.11.048.
Zhao, J., Cheng, Y.F., 2024. A phase field method for predicting hydrogen-induced cracking on pipelines. Int. J. Mech. Sci. 283, 109651. https://doi.org/10.1016/j.ijmecsci.2024.109651.
Zheng, J., Xu, W., Jia, G., et al., 2025. The mixing characteristics of natural gas and hydrogen based on the soave–redlich–kwong equation of state. Phys. Fluids 37 (7). https://doi.org/10.1063/5.0275084.
Zheng, J., Xu, W.Q., Jia, G.W., et al., 2024. Performance analysis of coaxial shear static mixer for hydrogen blending into natural gas. Int. J. Hydrogen Energy 78, 1275–1287. https://doi.org/10.1016/j.ijhydene.2024.06.389.
Zhuang, Z.K., Yan, J.T., Sun, C.L., et al., 2020. The numerical simulation of a new double swirl static mixer for gas reactants mixing. Chin. J. Chem. Eng. 28 (9), 2438–2446. https://doi.org/10.1016/j.cjche.2020.05.008.
Zidouni, F., Krepper, E., Rzehak, R., et al., 2015. Simulation of gas–liquid flow in a helical static mixer. Chem. Eng. Sci. 137, 476–486. https://doi.org/10.1016/j.ces.2015.06.052.